

# Fast manipulation of a quantum gas on an atom chip with a strong microwave field

Manon Ballu, Bastien Mirmand, Thomas Badr, H el ene Perrin and Aur elien Perrin  
*Universit e Sorbonne Paris Nord, Laboratoire de Physique des Lasers,  
 CNRS UMR 7538, 99 av. J.-B. Cl ement, F-93430 Villetaneuse, France*  
 (Dated: May 14, 2024)

We report on an experimental platform based on an atom chip encompassing a coplanar waveguide which enables to manipulate a quantum gas of sodium atoms with strong microwave fields. We describe the production with this setup of a very elongated degenerate quantum gas with typically  $10^6$  atoms, that can be prepared all along the cross-over from the three-dimensional to the one-dimensional regime depending on the atom number and trapping geometry. Using the microwave field radiated by the waveguide, we drive Rabi oscillations between the hyperfine ground states, with the atoms trapped at various distances from the waveguide. At the closest position explored, the field amplitude exceeds 5 G, corresponding to a Rabi frequency larger than 6 MHz. This enables fast manipulation of the atomic internal state.

## I. INTRODUCTION

Atom chips are a versatile technology for the manipulation of ultra-cold neutral atoms [1–7]. They primarily refer to surface-mounted structures enabling the production of magnetic traps of micrometric dimensions [3–7]. Microfabrication gives access to a large variety of magnetic potentials resulting from the set of current-carrying wires. It also enables to include waveguides radiating microwave fields near their surface [8]. The latter has proven to be an effective tool for the coherent manipulation of the internal states of atoms with a hyperfine structure, such as alkali atoms in their ground state [9, 10], opening a wide range of applications such as compact atomic clocks [11–14] or interferometers [9, 15, 16], spectroscopy of the elementary excitations of a quantum gas [17] or entanglement between quantum states [9, 18]. In these works, the microwave field is used either near resonance, driving coherent one-photon or two-photon Rabi oscillations with a long coherence time [8, 11], or far from resonance to dress the atomic states [13].

Another promising application of microwave fields for neutral atoms on a chip concerns the manipulation of the collisional properties of a quantum gas. It has been proposed that a microwave field could be used to tune the scattering length of alkali atoms near a microwave Feshbach resonance [19]. The field amplitude required for this application is however very large, on the order of several gauss. Microwave guides deposited on atom chips offer strong field amplitudes in the vicinity of the chip, providing an ideal platform for applications where a large field is required.

In this paper, we report on the manipulation of a sodium Bose-Einstein condensate confined in a magnetic microtrap with a strong microwave field produced by a coplanar waveguide in the immediate proximity of the atomic cloud. We observe fast coherent oscillations of the atomic states, driven by the large amplitude microwave field. We achieve a field amplitude exceeding 5 G. These results pave the way to fast manipulation of atomic states for applications in quantum technologies.

The paper is organized as follows: In Sec. II, we de-

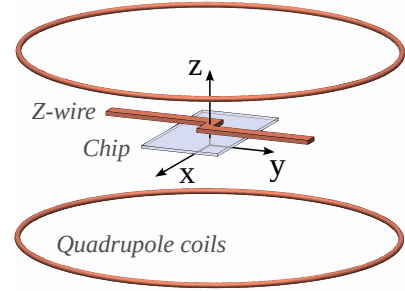


FIG. 1. Trapping elements layout and orientation. The on-chip trapping wires (with current flowing along the  $x$  direction) are located 4 mm above the zero point of the quadrupole field. The Z-wire that creates the intermediate trap lies above the chip (see Fig. 2 for details). Coils generating homogeneous magnetic fields are not shown.

scribe the atom chip design and present the different trapping potentials that can be obtained with our experimental platform. In Sec. III, we describe the different steps needed to produce a Bose-Einstein condensate. Finally in Sec. IV, we report the observation of fast coherent Rabi oscillations enabled by the strong microwave field. Additional technical details on the experimental sequence, the calibration of atom number in absorption imaging, the calibration of the static magnetic fields used to produce the magnetic trap, the microwave coupling amplitude and the transmission of the coplanar waveguide are given in Appendices.

## II. EXPERIMENTAL CONFIGURATION

The overall layout of our experimental configuration is depicted in Fig. 1. During the experimental sequence, three different magnetic traps are subsequently used to confine the atoms (see details in section III). Two coils of axis  $z$  in anti-Helmholtz configuration produce a spherical quadrupole magnetic trap. The atom chip lies in the horizontal plane approximately 4 mm above the center of

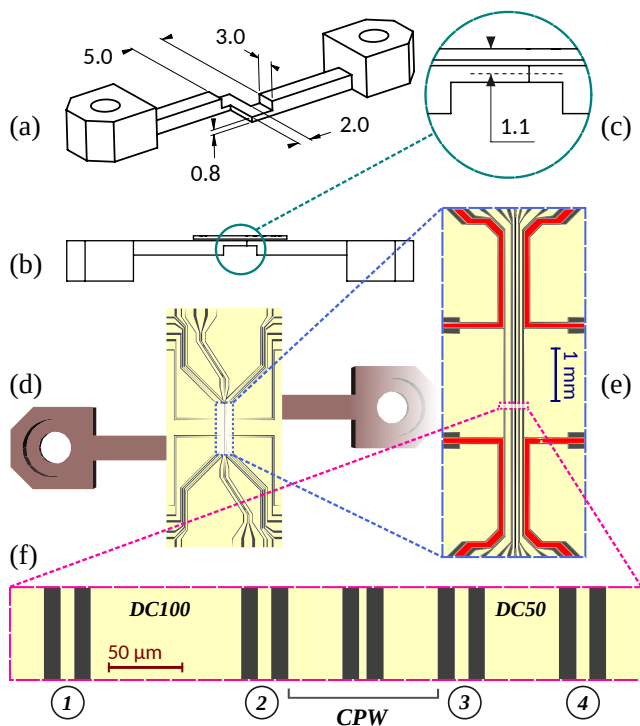


FIG. 2. (a) Drawing of the Z-wire for the intermediate trap. The dimensions of the central part are given in millimeters. (b) Position of the chip relative to the Z-wire. (c) The distance between the top surface of the chip and the median plane of the Z-wire is 1.1 mm. (d) Perspective top-view of the assembly. (e) Close-up view of the chip. For clarity, the four U-shaped wires are coloured in red. (f) Zoom in on the central part of the chip. The four RF tracks (circled numbers) are 10  $\mu\text{m}$  wide. The coplanar waveguide (CPW) consists of three conductors (37, 6 and 37  $\mu\text{m}$  wide respectively) separated by 10  $\mu\text{m}$  gaps. The two trapping wires ‘DC100’ and ‘DC50’ are 100  $\mu\text{m}$  and 50  $\mu\text{m}$  wide respectively.

the quadrupole trap, facing downwards. It is made of a silicon wafer of thickness 500  $\mu\text{m}$ , oxidized on a layer of thickness 20 nm. On this face, 2  $\mu\text{m}$ -thick microfabricated wires have been evaporated (see Fig. 2(d-e)). Two wires are colinear with the  $x$ -axis and will be referred to as ‘main trapping wires’ in the following: ‘DC50’ and ‘DC100’ with respective transverse widths 50  $\mu\text{m}$  and 100  $\mu\text{m}$ , see Fig. 2(f). Two pairs of U-shaped wires, or U-wires, of transverse width 100  $\mu\text{m}$  and spaced by 2 mm along the  $x$ -axis (in red in Fig. 2(e)) sit on both sides. In between the two main trapping wires, three wires colinear with the  $x$ -axis and of respective widths 37  $\mu\text{m}$ , 6  $\mu\text{m}$  and 37  $\mu\text{m}$  form a coplanar waveguide that induces a near-field microwave radiation. The geometry of the waveguide has been optimized for a good impedance matching between 1.5 and 2 GHz (see Appendix D).

Setting currents in one of the main trapping wire as well as in the U-wires and combining with homogeneous external bias fields produced by macroscopic coils leads to very elongated Ioffe-Pritchard magnetic traps

sitting below the atom chip plane [3, 4]. The external bias field has both a transverse component,  $\mathbf{B}_{\text{bias},\perp} = B_{\text{bias},y}\mathbf{e}_y + B_{\text{bias},z}\mathbf{e}_z$ , whose modulus  $B_{\text{bias},\perp}$  tunes the distance of the trap minimum to the main wire while the ratio  $B_{\text{bias},z}/B_{\text{bias},y}$  tunes its angular position, and a longitudinal component  $B_{\text{bias},x}\mathbf{e}_x$  which controls the value of the magnetic field at the trap minimum  $B_{\text{min}}$ .

This geometry results in an almost isotropic harmonic trapping in the transverse plane  $yz$  for low-field seeking atomic states. The longitudinal harmonic trapping is controlled independently from the current in the U-wires, that provide a weak curvature to the magnetic potential in the  $x$  direction. The longitudinal and transverse oscillation frequencies obtained from this geometry for the magnetic trap are very different, with a longitudinal frequency of the order of  $\omega_x/(2\pi) = 10$  to 25 Hz and a transverse frequency  $\omega_{\perp}/(2\pi)$  ranging between 1 and 10 kHz, depending on the parameters.

A millimeter-sized Z-shaped wire, or Z-wire, is placed 200  $\mu\text{m}$  above the top surface of the atom chip, see Fig. 1 and Fig. 2(a-d). The central bar of this Z-wire plays the role of the main trapping wire and its two side bars the role of longitudinal trapping in an intermediate compression step between the macroscopic quadrupole trap and the final microtrap, which have a very different trapping volume.

The external bias field is obtained from four independent macroscopic pairs of coils in Helmholtz configuration surrounding the vacuum chamber. Two of them are aligned along the  $x$  axis and contribute to  $B_{\text{bias},x}$  in an opposite way. This is necessary to either compensate partially the offset field created by the Z-wire along the  $x$ -axis, that would otherwise be too large and prevent reaching strong transverse trapping frequencies, or to increase the longitudinal field produced by the U-wires for reaching a value for  $B_{\text{min}}$  large enough to avoid Majorana losses. The third pair of coils along the  $y$ -axis sets the value of  $B_{\text{bias},y}$ . The last pair is provided by the quadrupole coils themselves, which can be switched to Helmholtz configuration with electromechanical switches. In the latter configuration they are used to set  $B_{\text{bias},z}$ .

### III. PRODUCTION OF A DEGENERATE BOSE GAS

In this section, we describe the steps taken to produce a Bose-Einstein condensate in the chip trap and examine the dimensionality regime depending on the atom number.

#### A. Overview of the first experimental steps

The experimental setup consists in three main vacuum chambers, respectively for the atomic source, the magneto-optical trap and the science chamber, separated

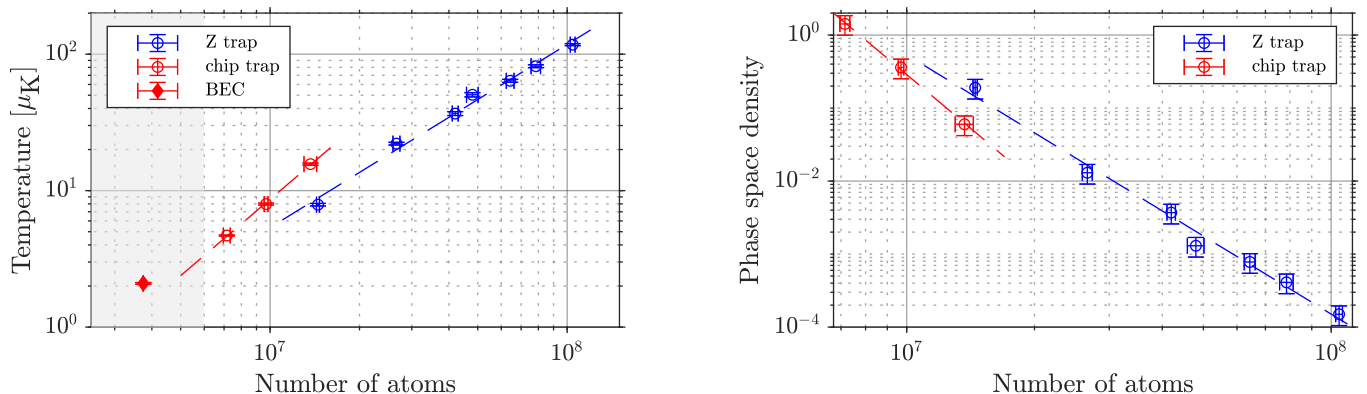


FIG. 3. **Left** - Evolution of the atom number and temperature during the two forced evaporative cooling ramps, respectively in the Z-trap (blue circles) and in the atom chip trap (red circles). The shaded area indicates the region where the system reaches Bose-Einstein condensation. The red filled circle corresponds to a degenerate gas and the temperature is evaluated from its thermal fraction. **Right** - Same results in terms of phase space density and atom number. The evaluation of the phase space density relies on a modelling of the trapping potential (see Appendix B).

by long tubes maintaining a pressure difference. A hot beam of sodium atoms is prepared in an oven: atoms in the liquid phase are maintained at a temperature of 235°C at the bottom while the upper and output part, where the gaseous phase is concentrated, is heated up to 275°C. Relying on a permanent-magnet Zeeman slower [20, 21], we decelerate the atoms and load them into a magneto-optical trap. The cold gas is then compressed and further cooled in an optical molasses. A quadrupole magnetic trap is subsequently switched on to capture atoms in the  $|F = 1, m_F = -1\rangle$  state, where  $F$  is the total angular momentum of an atom in its ground state and  $m_F$  its projection along the local magnetic field direction. Taking advantage of a magnetic transport with a sequence of 13 pairs of coils [22, 23], we move the trapped gas over 60 cm up to the science chamber. At the end of the procedure, typically  $10^9$  atoms are confined at a temperature of 130 μK in the spherical quadrupole trap 4 mm below the surface of the atom chip (see Fig. 1).

The route from this initial trap to the evaporation to degeneracy in the atom chip trap proceeds in two main steps, each of which is divided into three stages: transfer, compression and evaporative cooling (see Fig. 10 of Appendix A for an overview of the experimental sequence and the stage labels). The first step brings the atoms from the quadrupole trap to an intermediate trap based on the Z-wire for a better mode matching to the tight and elongated final microtrap, that is loaded during the second step and where cooling to degeneracy is performed.

### B. First step: Transfer to the intermediate Z-trap and pre-cooling stage

The intermediate magnetic trap configuration is an elongated Ioffe-Pritchard trap denoted ‘Z-trap’ in the following. It relies on the field produced by a current of 110 A flowing in the Z-wire combined with a bias field as

introduced in Sec. II. The  $x$ -component of the bias field is chosen to fix a minimum field of order 2 G, preventing Majorana losses.

The transfer from the initial quadrupole trap to the intermediate Z-trap is performed in two parts: a fast transfer to a tighter quadrupole trap resulting from the Z-wire, step (1a) of Fig. 10, followed by a slower transfer to the Ioffe-Pritchard trap with a non-zero magnetic minimum (1b). The first part is completed in 50 ms through a linear increase of the current in the Z-wire from 0 to 110 A, while the current of the quadrupole coils is decreased linearly down to zero. Simultaneously, we ramp up  $B_{\text{bias},x}$  and  $B_{\text{bias},y}$  in two successive linear ramps of 25 ms each. Near the end of the ramps, the trap is strongly deformed which leads to significant atomic losses. At the end of this part of the transfer, the center of the trap is close to its initial position and  $B_{\text{min}} = 0$ . At this stage we are left with 55% of the initial atoms.

The second part (1b) is much slower. During the next 500 ms, we continue to increase both  $B_{\text{bias},x}$  and  $B_{\text{bias},y}$ , which brings the atoms closer to the surface of the atom chip, enhances the transverse magnetic gradients and sets the magnetic field minimum at about 2 G, resulting in a Ioffe-Pritchard configuration. At this point, the cloud size is large enough for the most energetic atoms to collide with the atom chip surface. For the next compression stage of 4 s, we continue to move the trap upwards and compress it very slowly, until the collision rate becomes favorable to start a forced evaporative cooling ramp.

The blue circles in Fig. 3 show the temperature (left) or phase space density (right) as a function of the atom number, measured along the subsequent 6 s evaporation phase (1c), which takes place in a trap located at a distance of about 550 μm from the atom chip surface. Appendix C explains how we have calibrated the atom number obtained from the absorption imaging sequence while Appendix B gives details on our estimation of the phase space density. To expel the most energetic atoms from

the magnetic trap, we rely on a radiofrequency (RF) field produced by a coil located just above the atom chip. We start evaporation with a frequency  $\nu_{\text{ev}}$  of 20 MHz and linearly ramp it down to 3 MHz.

### C. Second step: Transfer to the atom chip trap and final evaporation

The transfer from the Z-trap to the atom chip trap is performed in 350 ms. We first linearly ramp up the current in the DC100-wire and the U-wires to their final values in 100 ms (2a). In the next 250 ms we linearly decrease the current in the Z-wire while linearly ramping down  $B_{\text{bias},x}$  and  $B_{\text{bias},y}$  (2b). Note that 5 ms before the end of the ramp,  $B_{\text{bias},x}$  vanishes and then changes sign. This procedure allows us to increase the offset field produced by the U-wires along  $x$  and maintain the magnetic field minimum between 1 and 2 G during the whole transfer. At this point the atoms are confined at a distance of 210  $\mu\text{m}$  from the chip surface.

We then move up and compress the trap further by linearly increasing  $B_{\text{bias},y}$  to its final value in 100 ms (2c). The distance of the atoms to the chip surface is now 120  $\mu\text{m}$ , the measured transverse trapping frequencies reach  $\omega_{\perp}/(2\pi) = 3.2$  kHz and the magnetic field minimum is now  $B_{\text{min}} = 1$  G. During the transfer and compression stages, we also keep an RF-knife at a frequency  $\nu_{\text{ev}} = 3$  MHz. During the next 500 ms (3b), we proceed to the final forced evaporative cooling ramp from 3 MHz down to 750 kHz where we reach degeneracy and observe Bose-Einstein condensation. The red circles in Fig. 3 summarize our results in term of temperature (left), phase space density (right) and atom number during this last evaporation stage. We obtain condensates with typically  $10^6$  atoms at a temperature of 1  $\mu\text{K}$ .

### D. 3D-1D crossover

Adjusting the final frequency of the forced evaporative cooling ramp allows us to decrease the temperature of the system even further. At some point the thermal fraction becomes negligible and in order to evaluate the temperature of the gas, we cannot rely on the usual time-of-flight technique. Instead, we take advantage of the very elongated nature of the system: it is responsible for visible density fluctuations along the long direction of the trap that develop during time-of-flight expansion [24]. The power spectrum of these fluctuations contains information on the temperature of the system [25, 26]. These effects become significant as soon as the energy scales of the gas, chemical potential and temperature, approach the transverse trapping energy  $\hbar\omega_{\perp}$ , where  $\hbar$  is the reduced Planck constant. In this case, the system enters the so-called one-dimensional-three-dimensional crossover (1D-3D), where the physics is mainly governed by the longitudinal characteristics of the gas. The gas cannot be con-

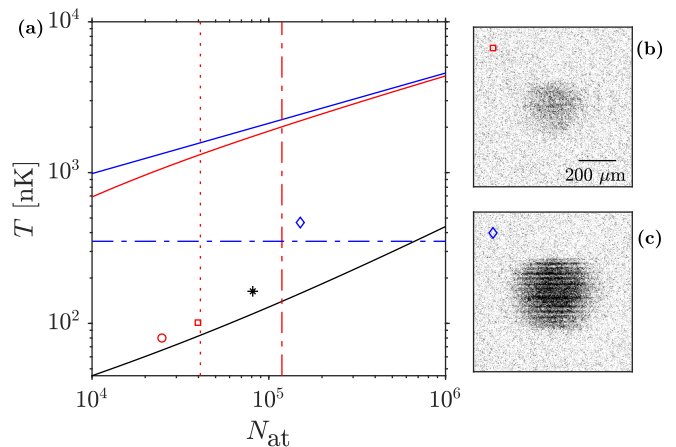


FIG. 4. (a) Temperature and atom number of the system in the degenerate regime for different final frequencies of the evaporative cooling ramp (red open circle, red filled circle, black star and blue diamond). The blue line corresponds to the usual three-dimensional temperature threshold for Bose-Einstein condensation  $k_B T_c = 0.94 \hbar \bar{\omega} N^{1/3}$  [27] which assumes  $k_B T_c \gg \hbar \bar{\omega}$  with  $\bar{\omega} = (\omega_x \omega_{\perp}^2)^{1/3}$ . The red line gives the exact calculation for  $T_c$  in our elongated geometry where the semi-classical approximation does not always hold. The red dashed dotted line corresponds to the limit  $\chi = \chi_{\text{cross}}$  (see text) and the blue dashed dotted line to  $k_B T = \hbar \omega_{\perp}$ . The red dotted line corresponds to the limit  $\mu = 2\hbar \omega_{\perp}$ . Finally, the black line corresponds to the limit where the thermal coherence length of the gas is equal to the longitudinal radius of the system. (b) and (c) show typical examples of the gas after 10 ms time of flight and obtained with absorption imaging.

sidered as a true Bose-Einstein condensate anymore but is rather referred to as a quasicondensate, where longitudinal thermal excitations population is significant compared to the true ground state population.

We first examine the criterion involving the chemical potential  $\mu$ . In order to evaluate in which regime the gas is prepared in the 1D-3D crossover, we use the parameter  $\chi = N a a_{\perp} / a_x^2$  introduced in Ref. [28], where  $a$  is the scattering length describing the two-body interaction between the atoms and  $a_{x,\perp} = \sqrt{\hbar/m\omega_{x,\perp}}$  are the harmonic oscillator lengths along the respective trap axes, with  $m$  the atom mass. According to Ref. [28], the boundary between the 3D and 1D regimes occurs for  $\chi = \chi_{\text{cross}} \simeq 3.73$ . Another criterion is obtained by comparing directly the chemical potential  $\mu$  to  $\hbar\omega_{\perp}$ .  $\mu$  is always larger than  $\hbar\omega_{\perp}$  due to the contribution of the zero-point energy  $\hbar\omega_{\perp}$  of the transverse ground state. The cross-over thus occurs when  $\mu$  is of order  $2\hbar\omega_{\perp}$ . The chemical potential  $\mu$  can be evaluated by solving [28]

$$32 \left( \frac{\mu}{\hbar\omega_{\perp}} - 1 \right)^3 \left( \frac{\mu}{\hbar\omega_{\perp}} + 4 \right)^2 = (15\chi)^2. \quad (1)$$

The boundary between the 1D and 3D regimes is represented in Fig. 4 using these two criteria.

We now examine the criterion on the temperature. The

1D regime is reached when  $k_B T < \hbar\omega_\perp$  where  $k_B$  is the Boltzmann constant and  $T$  is the temperature of the system. As mentioned above,  $T$  can be extracted from the analysis of the power spectrum of the density fluctuations that arise during the time of flight expansion. To this aim, we repeat the experiment about 50 times in the same conditions in terms of atom number and final frequency of the evaporative cooling ramp and let the atoms expand for 10 ms. The analysis of the pictures recorded by absorption imaging gives access to the power spectrum of the density fluctuations that we compare to the analytical model detailed in [26]. It allows us to extract the thermal coherence length of the gas  $\ell_c = 2\hbar n_0/k_B T$  where  $n_0$  is the peak density of the longitudinal profile integrated along the transverse directions.

In Fig. 4, we show the results obtained for four different final values of the final frequency at the end of the evaporative cooling ramp, in a trap where  $\omega_x = 2\pi \times 20$  Hz and  $\omega_\perp = 2\pi \times 7.3$  kHz. Comparing the atom number to the one set by  $\chi_{\text{cross}}$  and the temperature to  $\hbar\omega_\perp/k_B$ , we observe that our system smoothly crosses the 1D-3D crossover. For the two coldest samples, the estimated thermal coherence length  $\ell_c$  gets very close to the longitudinal radius of the gas  $R_x = a_x^2/a_\perp \sqrt{2(\mu/\hbar\omega_\perp - 1)}$  (see [28]). This means that the system reaches the crossover to a finite size one-dimensional Bose-Einstein condensate, where the ground state population becomes preponderant compared to thermal excitations.

#### IV. OBSERVATION OF FAST COHERENT RABI OSCILLATIONS

Once the degenerate gas is prepared in the chip trap, we can manipulate its internal state using the strong microwave field produced in the vicinity of the microwave guide.

##### A. Moving the cloud below the microwave waveguide

The quantum gas is prepared at the vertical of the DC100-wire. On the other hand, the microwave waveguide produces an oscillating magnetic field whose amplitude decreases with the distance to the center of the waveguide. In order to benefit from large microwave amplitudes, we need to move the center of the atom chip trap closer to the waveguide. For this, we change the relative amplitudes  $B_{\text{bias},y}$  and  $B_{\text{bias},z}$  of the transverse bias field  $\mathbf{B}_{\text{bias},\perp}$  in order to rotate the position of the center of the trap around the main trapping wire.

Starting from the final position of the trap described in III C, we linearly increase  $B_{\text{bias},z}$  while decreasing  $B_{\text{bias},y}$  in 100 ms (3a), just before the final evaporative cooling ramp (3b). In Fig. 5, we show different final positions that can be reached depending on the final components of  $\mathbf{B}_{\text{bias},\perp}$ . We also indicate the value of the

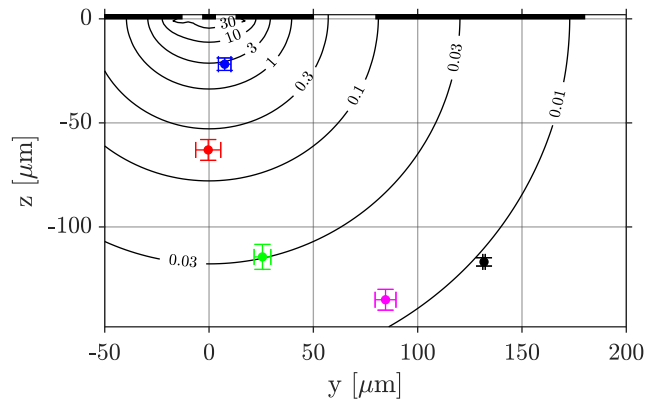


FIG. 5. Position of the center of the atom chip trap for different values of  $\mathbf{B}_{\text{bias},\perp}$ . On the upper edge of the figure, the main trapping wire DC100 and the three parts of the microwave waveguide are represented as black rectangles. The black lines correspond to the isomagnetic lines as deduced from a static model for the microwave waveguide (see text). The modulus of the magnetic field is indicated on each line (in gauss).

amplitude of the microwave field that can be deduced from a simple model which assumes static currents in the waveguide, as follows. The skin depth in a gold wire for a signal around 1.77 GHz is about 1.8  $\mu\text{m}$ , and we assume a homogeneous current density in the central wire. For the two ground wires, the current flows in the opposite direction with half the amplitude and we assume a homogeneous current density on the two inner edges facing the central wire, spread over a width set by the skin depth.

The positions shown in Fig. 5 are deduced from a model which takes into account the geometry of the DC100- and U-wires assuming a homogeneous current density. The two components of  $\mathbf{B}_{\text{bias},\perp}$  have been measured from the Zeeman shift that they induce on the hyperfine atomic transition (see Appendix B).

##### B. Calibration of the microwave field amplitude

Once the atoms have been brought in the vicinity of the waveguide, they can be manipulated with a strong microwave field. The microwave field amplitude can be estimated from the input current and a modelling of the waveguide. A more precise calibration is performed by a direct measurement of the field amplitude using the atomic cloud as a local probe, which also gives access to the amplitude of the different components of the microwave polarization. To this aim, we drive Rabi oscillations between the trapped  $|F = 1, m_F = -1\rangle$  state and one of the  $|F = 2, m_F = -2, -1, 0\rangle$  states that are accessible due to selection rules. In order to observe clear oscillations of the population in the initial state, we need to choose a Rabi coupling larger than the chemical potential of the trapped gas, to limit the loss of co-

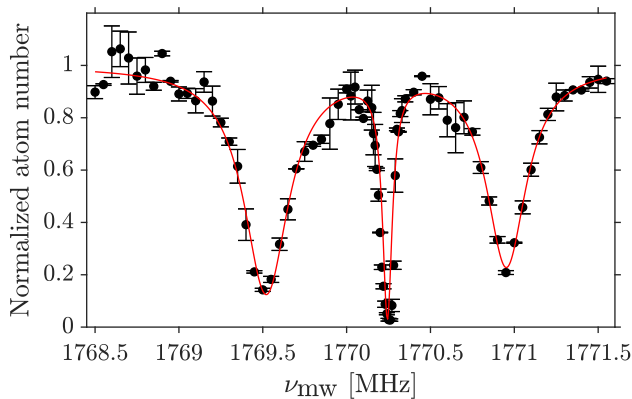


FIG. 6. Microwave spectroscopy of the trapped atoms (see text for the exact experimental procedure). The three peaks correspond to the different polarisations present in the microwave field. The distance between the peaks is used to determine  $B_{\min}$  precisely. Here we find  $B_{\min} = 1.07$  G. The red line is a fit including three Lorentzian peaks.

herence due to the inhomogeneous magnetic field in the trap, but smaller than the Zeeman splitting to resolve a single two-level transition. The expression of the expected Rabi frequency for a given hyperfine transition is detailed in Appendix E. Its relation to the microwave amplitudes  $\Omega_{\pm,0} = -|g_F|\mu_B B_{\pm,0}/\hbar$  in units of frequency, where  $B_{\pm}$  and  $B_0$  are the microwave field components, depends on the matrix elements of the transition. Briefly, it is equal to the microwave amplitude  $\Omega_+$  for the  $|F=1, m_F=-1\rangle \rightarrow |F=2, m_F=0\rangle$  transition addressed by the  $\sigma^+$  component of the polarization, to  $\sqrt{3}\Omega_0$  for the  $|F=1, m_F=-1\rangle \rightarrow |F=2, m_F=-1\rangle$   $\pi$  transition and to  $\sqrt{6}\Omega_-$  for the  $|F=1, m_F=-1\rangle \rightarrow |F=2, m_F=-2\rangle$   $\sigma^-$  transition. The chemical potential is  $h \times 20$  kHz or below for the typical atom numbers and trap geometries that we have investigated. The Zeeman frequency splitting is on the order of 700 kHz at the trap bottom, such that we aim for Rabi frequencies on the order of 100 kHz.

At each trap position shown in Fig. 5, we adjust the amplitude of the current in the microwave waveguide in order to observe clear oscillations of the population of the trapped  $|F=1, m_F=-1\rangle$  state while scanning the microwave pulse duration. A typical example is shown in Fig. 7. We keep the atoms in the trap for 20 ms after the pulse in order to get rid of the  $F=2$  population. We then fit the frequency of the oscillations in order to determine the Rabi frequency, and thus the amplitude of the component of the microwave field which drives the oscillations. In the case of Fig. 7, the microwave is resonant with the  $|F=1, m_F=-1\rangle \rightarrow |F=2, m_F=-2\rangle$  transition and we find  $|B_-| \simeq 46$  mG. We also observe a damping of the oscillations that we attribute to a gradient of amplitude of the microwave field over the vertical size of the cloud and to the inhomogeneity of the magnetic field in the trap.

We have repeated this procedure for all the trap positions shown in Fig. 5, calibrating  $|B_-|$  and  $|B_+|$ . Even

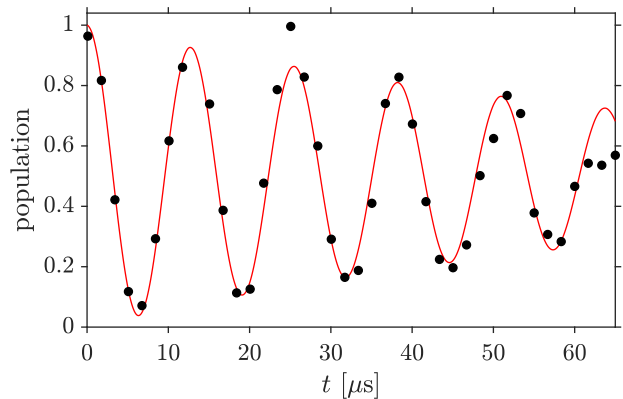


FIG. 7. Rabi oscillations of the population of the  $|F=1, m_F=-1\rangle$  state coupled to the  $|F=2, m_F=-2\rangle$  state with the  $\sigma^-$  component of the microwave field. From the fit of the Rabi frequency, which includes an exponential damping of the oscillations, we deduce a microwave amplitude  $|\Omega_-| \simeq 2\pi \times 32$  kHz. The damping of the oscillations is due to a gradient of the microwave field amplitude with the distance from the waveguide and to magnetic inhomogeneity in the trap.

though we observe a small coupling due to effect of  $|B_0|$  for a long pulse duration (see Fig. 6), its contribution is much smaller. This can be understood from the static model for the microwave waveguide introduced in IV A. It predicts that the polarization of the field should be linear and orthogonal to the  $x$  axis. Since the main trap axis is slightly tilted in the  $(xy)$  plane compared to the  $x$  axis, we still expect a faint contribution from the  $\pi$  polarization component of the microwave field, with respect to the quantization axis set by the static field, but very small compared to the other two.

In order to compare the results obtained at different positions, we have rescaled the measured microwave amplitude  $|\Omega_{+,-}|$  assuming that it depends linearly on the amplitude of the current in the microwave waveguide. The results are shown in Fig. 8, the color code matching the one of Fig. 6. We observe an algebraic decay of the amplitude of the coupling with the distance  $d = \sqrt{x^2 + y^2}$  to the center of the microwave waveguide with a power close to  $-2$ . We also see that the amplitudes of the  $\sigma^-$  and  $\sigma^+$  components of the microwave field are not exactly equal at a given position and that their relative strength depends on the distance. This effect is not captured by the simple static model of the waveguide. The measured values of  $|\Omega_{+,-}|$  before rescaling are given in Table I.

### C. Large amplitude coherent oscillations

We have studied the evolution of the hyperfine state population in the case where the trap is brought at its closest position to the waveguide (blue point in Fig. 5), using a strong microwave amplitude. With these large

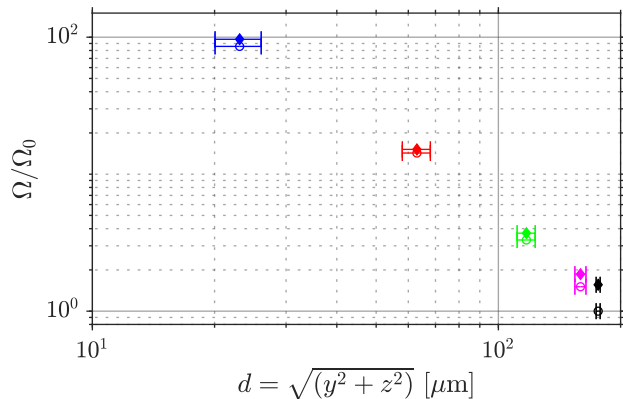


FIG. 8. Relative microwave amplitudes  $|\Omega_+|$  (Filled diamond) and  $|\Omega_-|$  (circle) as a function of the distance to the center of the waveguide, normalized by the value of  $|\Omega_-|$  at the initial position, the farthest from the waveguide. The color code is the same as in Fig. 5.

$d$ [ $\mu\text{m}$ ]	Power [dBm]	$ \Omega_- /2\pi$ [kHz]	$ B_- $ [mG]	$ \Omega_+ /2\pi$ [kHz]	$ B_+ $ [mG]
176	36	43	61	67	96
	32	27	39		
159	32	40	57	51	73
	23	15	21		
117	23	32	46	36	51
63	23	137	200	146	210
	18	78	110		
23	13	262	370	294	420
	18	461	660		

TABLE I. Raw data used to produce Fig. 8. The distance  $d$  of the trap position to the main trapping wire is computed assuming a homogeneous current density in the atom chip wires. The MW power is measured at the output of the amplifier, before the coplanar waveguide. The amplitude  $|\Omega_-|$  and  $|\Omega_+|$  and MW amplitudes  $|B_-|$  and  $|B_+|$  are deduced from a fit of the population oscillations between the trapped  $|F = 1, m_F = -1\rangle$  state and the  $|F = 2, m_F = -2\rangle$  and  $|F = 2, m_F = 0\rangle$  respectively (see for instance Fig. 7). The MW frequency is adapted in to be resonant with the probed transition.

amplitudes, we observe rapid coherent oscillations of the population of the trapped  $|F = 1, m_F = -1\rangle$  state as shown in Fig. 9. In this case, both the  $\sigma^+$  and  $\sigma^-$  polarization contribute since the amplitudes  $|\Omega_{+,-}|$  are larger than the Zeeman splitting. Adjusting our data with the model described in Appendix E and assuming a perfect linear polarization  $B_{\text{mw}} \cos(\omega t) \mathbf{e}_z$ , we deduce  $|\Omega_-| = |\Omega_+| \simeq 2\pi \times 2.7 \text{ MHz}$  which corresponds to  $|B_-| = |B_+| \simeq 3.8 \text{ G}$  or equivalently  $B_{\text{mw}} = 5.4 \text{ G}$ . Such a large field enables a fast manipulation of the internal state, as the spin can be flipped from  $F = 1$  to  $F = 2$  in 75 ns only.

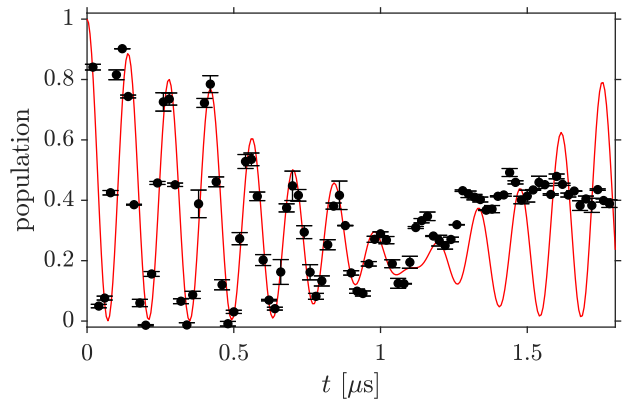


FIG. 9. Evolution of the population of the  $|F = 1, m_F = -1\rangle$  trapped state coupled to the  $F = 2$  states with a large amplitude microwave field resonant with the  $|F = 1, m_F = -1\rangle \rightarrow |F = 2, m_F = -2\rangle$  transition. The red line corresponds to theoretical expectations for a static field of 1 G and a linearly polarized microwave field with  $|\Omega_-| = |\Omega_+| \simeq 2\pi \times 2.7 \text{ MHz}$ . Damping is not taken into account in the model.

## V. CONCLUSION

In this paper we have described the production of degenerate quantum gases of sodium atoms in a magnetic microtrap relying on an atom chip. The latter encompasses a coplanar waveguide that we use to manipulate the hyperfine state of the trapped atoms thanks to a large amplitude microwave field. We observe coherent Rabi oscillations of the atomic population that allow us to determine the corresponding Rabi coupling and hence the amplitude of the microwave field. Depending on the distance of the magnetic trap minimum to the coplanar waveguide and on the microwave power used, we can tune the Rabi coupling from a few tens of kHz up to 6.6 MHz.

Such a large coupling can be interesting for quantum technology applications where fast manipulation of the atomic spin states are needed. It also allows for the realization of adiabatic potentials relying on microwave fields as already demonstrated with radiofrequency fields [29]. In this case, effects beyond the rotating wave approximation should be negligible [30]. Another interesting application concerns the possibility to address molecular resonances as explained for alkali atoms in [19] and recently demonstrated for rubidium atoms [31]. Close to the resonance, the scattering length of the atoms is expected to be modified as is the case with static magnetic field Feshbach resonances. Since the width of the resonance depends on the square of the microwave field amplitude, working with large amplitude microwave fields would allow for finer tuning of the scattering length.

## ACKNOWLEDGMENTS

We thank Romain Dubessy for the design of the coplanar waveguide and for helpful discussions, Matthias

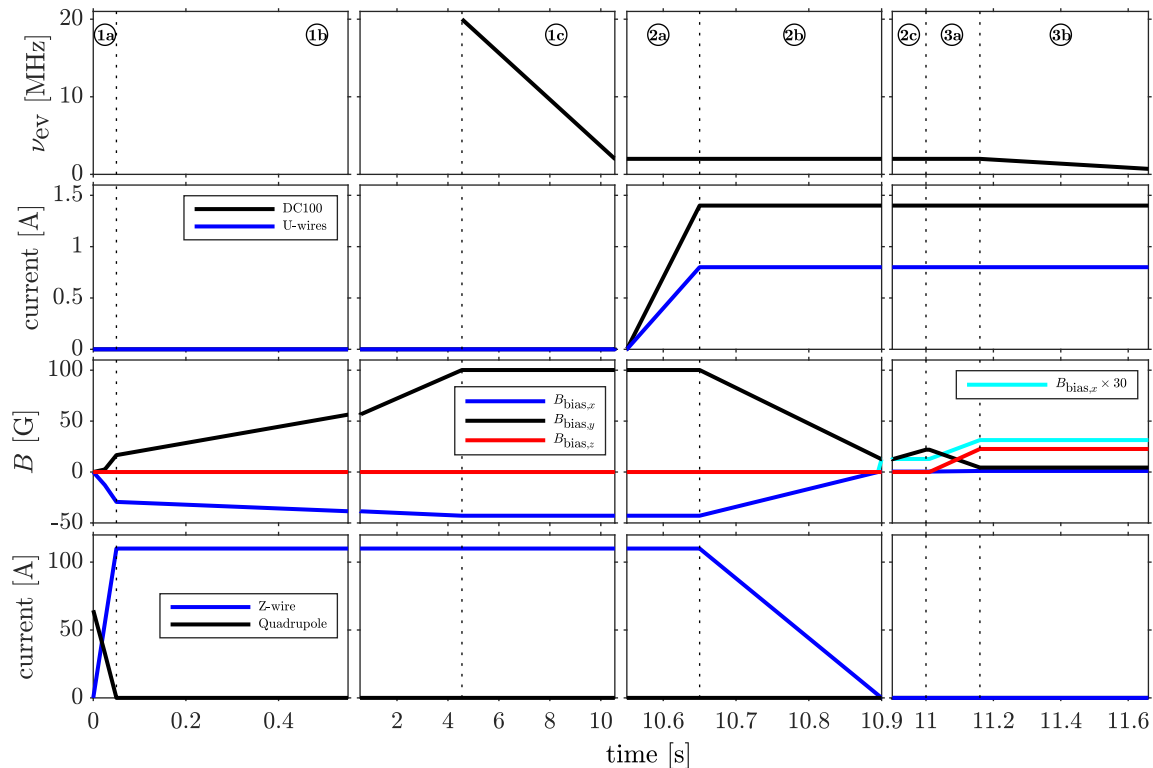


FIG. 10. Timeline of the experimental sequence. From bottom to top, currents in the Z-wire and the quadrupole coils,  $x$ ,  $y$  and  $z$  components of  $B_{\text{bias}}$ , currents in the main trapping wire and U-wires and frequency  $\nu_{\text{ev}}$  of the evaporative cooling ramp. The sequence is split into three main steps, each divided in substeps: **1a** Transfer from the quadrupole trap to the intermediate Z-trap - **1b** Compression of the Z-trap - **1c** Z-trap evaporative cooling ramp - **2a** Switch on of the main trapping wire and U-wires current - **2b** Transfer to the atom chip trap - **2c** Compression of the atom chip trap - **3a** Transport to below the microwave waveguide - **3b** Final evaporative cooling ramp to degeneracy.

Stüwe and Jörg Schmiedmayer (TU Wien) for the atom chip fabrication, Thibaut Vacelet (Observatoire de Paris - LERMA (CTOP)) for cutting and performing the wire-bonding on the atom chip. We also thank Jeanne Solard (USPN), Pascal Filloux and Christophe Manquest (USPC) for their assistance in the early stages of the technical development and Yann Charles (LSPM) for performing numerical simulations of the heat conductance of the trapping wires. This work has been supported by the Agence Nationale de la Recherche (ANR) under the projects ‘ANR-21-CE47-0009-03’ and ‘ANR-22-CE91-0005-01’.

### Appendix A: Experimental sequence

Fig. 10 summarizes the timeline of the experimental sequence for the currents, bias fields and evaporative cooling frequency  $\nu_{\text{ev}}$  used to bring the atoms from the initial quadrupole trap to the atom chip trap and then close to the coplanar waveguide. The values shown here correspond to the blue position in Fig. 5.

### Appendix B: Characterization of the static magnetic configuration

The peak phase-space density in Fig. 3 is estimated from the measured atom number  $N$  and temperature  $T$ , and from the knowledge of the magnetic landscape. It is equal to  $n(\mathbf{r}_0)\lambda_T^3$ , with

$$n(\mathbf{r}_0) = \frac{N \exp[-V(\mathbf{r}_0)/k_B T]}{\int d\mathbf{r} \exp[-V(\mathbf{r})/k_B T]} \quad (\text{B1})$$

the density at the position  $\mathbf{r}_0$  of the magnetic field minimum and

$$\lambda_T = \sqrt{\frac{2\pi\hbar^2}{mk_B T}} \quad (\text{B2})$$

the thermal de Broglie wavelength. The magnetic potential  $V$  seen by the trapped atomic state is calculated numerically from the geometry of the different wires involved and relying on an independent calibration of  $\mathbf{B}_{\text{bias}}$  explained below. Each wire geometry is approximated by a succession of rectangular cuboid with homogeneous current density. We have checked that these numerical predictions are in good agreement with the measured oscillation frequencies for various trap parameters.

The experimental sequence used to calibrate the different components of  $\mathbf{B}_{\text{bias}}$  is the following : we prepare a Bose-Einstein condensate and switch off abruptly all the fields contributing to the magnetic potential apart from the field component that we want to calibrate. After a time of flight of 5 ms, we switch on the microwave field for 100  $\mu\text{s}$  and scan its frequency. Since the atoms are trapped in the  $|F = 1, m_F = -1\rangle$  state, we can only couple to the  $|F = 2, m_F = -2, -1, 0\rangle$  states depending on the microwave polarisation because of selection rules. The resonance frequencies are shifted due to the Zeeman effect  $\Delta\nu = |g_F(m_1 + m_2)|\mu_B B/h$  where  $|g_F| = 1/2$  is the hyperfine Landé g-factor,  $\mu_B$  the Bohr magneton,  $m_{1,2}$  the projections of the total spin for the initial and final states and  $B$  is the modulus of the total magnetic field that remains after the trap switch off. Note that  $B$  contains the contribution of the Earth magnetic field in addition to the field component that we want to calibrate. We finally record the population of the  $F = 2$  state with absorption imaging. The frequencies corresponding to the peak population correspond to resonances from which we deduce  $B$ . Repeating the experiment for different currents in the external coils and fitting all the results together we deduce the relation between each magnetic field component and the current in the external coils. Note that we also let the three components of Earth magnetic field (and possible other stray fields) as free parameters. The modulus of the magnetic field we estimate for this contribution is 0.55 G which is close to the Earth magnetic field (0.47 G), such that stray fields at the position of the atoms remain limited.

A similar technique can be used to precisely determine  $B_{\text{min}}$ . We shine the microwave field on the trapped atoms during 200  $\mu\text{s}$  and wait for 20 ms before switching off the confinement in order to let the high-field seeker  $F = 2$  atoms be expelled by the magnetic potential. Scanning the frequency of the microwave field and detecting the remaining population in  $F = 1$ , we can clearly distinguish three resonances corresponding to the different polarizations of the microwave field as shown in Fig. 6. The frequency difference between the resonances gives access to  $B_{\text{min}}$ .

### Appendix C: Simulations of the effective cross section for absorption imaging

Absorption imaging relies on the knowledge of the cross section  $\sigma$  describing the interaction between the imaging beam and the atoms [32]. In the case of a two-level atom, we can write

$$\sigma = \frac{\sigma_0}{1 + 4(\Delta/\Gamma)^2 + I/I_{\text{sat}}} \quad (\text{C1})$$

where  $\sigma_0 = \hbar\omega\Gamma/2I_{\text{sat}}$  is the resonant cross section,  $\omega/2\pi$  is the laser frequency,  $\Delta = \omega - \omega_{\text{at}}$  is the laser detuning from the atomic resonance of frequency  $\omega_{\text{at}}$ ,  $\Gamma \simeq 2\pi \times 9.79$  MHz is the natural linewidth of the excited state,  $I$

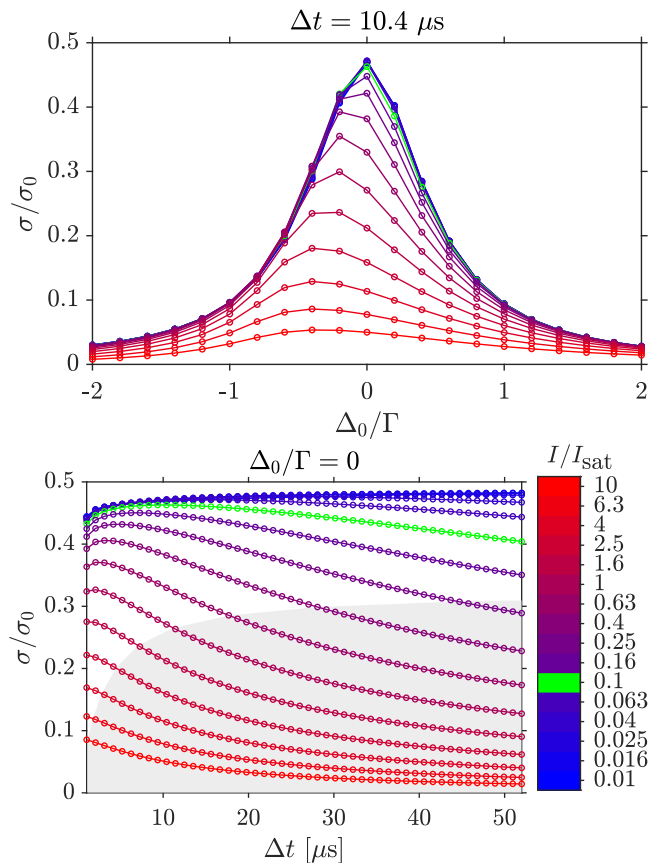


FIG. 11. **Top** - Effective absorption cross section of the imaging beam in units of the resonance cross section  $\sigma_0$  deduced from the optical Bloch equations for a fixed pulse duration as a function of the imaging beam detuning  $\Delta_0$  in units of the line width  $\Gamma$ . **Bottom** - Same quantity for a fixed imaging beam detuning  $\Delta_0/\Gamma = 0$  as a function of the imaging pulse duration  $\Delta t$ . The shaded area indicates the region where the signal saturates the CCD sensor of the camera. In both graphs, each curve corresponds to a different imaging beam intensity.

is the laser intensity and  $I_{\text{sat}} = 6.26 \text{ mW cm}^{-2}$  is the saturation intensity.

Sodium atoms are alkali atoms. Their hyperfine structure encompasses 8 levels in the ground state. The first excited state is a fine structure doublet and only the  $D_2$  line, including 16 levels, presents cycling transitions [33]. The excited state structure is not very large compared to  $\Gamma$  which makes the two-level atom approximation relatively inaccurate. Moreover, sodium atoms are quite light which means that the Doppler shift  $\Delta\omega_{\text{Dop}} \simeq 2\pi \times 50$  kHz associated with the absorption of a single photon is not negligible. This limits to a few hundreds the number of photons that can be scattered by an atom from the imaging beam before becoming off-resonant and in turn sets an upper bound on the pulse duration of a few  $\mu\text{s}$ .

In order to have a better insight of the performance of the absorption imaging setup, we have solved the optical Bloch equations taking into account the 24 electronic lev-

els involved within the  $D_2$  line. The Doppler shift due to the absorption of photons is taken into account through a time-dependent detuning  $\Delta(t)$

$$\Delta(t) = \Delta_0 - \Delta_{\text{Dop}} \int_0^t \Gamma \rho_{ee} dt \quad (\text{C2})$$

where  $\Delta_0$  is the laser detuning with respect to the  $F = 2 \rightarrow F' = 3$  transition, and  $\rho_{ee} = \sum_{F'=0...3} \sum_{m_{F'}=-F'} \rho_{F',m_{F'};F',m_{F'}}$  corresponds to the total population of the excited states. Hence  $\Gamma \rho_{ee}(t)$  is the total scattering rate.

In the experiment, the atoms occupy the  $|F = 1, m_F = -1\rangle$  state right before the magnetic trap is switched off. After time of flight, they are repumped to the  $F = 2$  states thanks to a short laser pulse at resonance with the  $F = 1 \rightarrow F' = 2$  transition. The repumper beam is oriented along the  $x$  axis and circularly polarized. Right after this pulse, we shine another laser beam oriented along the  $y$  axis and linearly polarized in the  $(xz)$  plane. Relying on the model described above, we have calculated the effective cross-section for our imaging sequence. The results are shown in Fig. 11. We see that the optimum imaging pulse duration depends on the laser intensity and that the largest effective cross-section is about  $0.45\sigma_0$ . In order to maximize the signal to noise ratio without saturating the camera, we have to work with an intensity corresponding to a fraction of the saturation intensity and then the optimum pulse duration lies around  $10 \mu\text{s}$ .

We have checked that the effective cross-section evaluated from these calculations is in good agreement with a careful calibration of the atom number performed from the expansion of Bose-Einstein condensates during a time of flight. The radii of the cloud scale according to equations derived in [34] which are independent of the atom number. The initial radii however depends on the atom number through the chemical potential. Comparing the expansion of clouds with different atom number and originating from different trap geometry, we could check that the experimental effective cross-section is about  $0.4\sigma_0$ .

We have also checked with the same calculations that it should be possible to increase the optimal effective cross-section to about  $0.9\sigma_0$  by orienting the repumper and the imaging beams along the same direction and sharing the same circular polarization. This is currently not possible on our setup but this is a clear direction for improvement in the future.

#### Appendix D: Scattering parameters of the coplanar waveguide

Using a commercial vector network analyzer, we have characterized the spectral response of the full circuit of the coplanar waveguide by measuring its  $S_{11}$  and  $S_{21}$  scattering parameters (see Fig. 12). The amplitude reflection (resp. transmission) parameter  $S_{11}$  (resp.  $S_{21}$ )

corresponds to the ratio of the reflected (resp. transmitted) signal to the incident signal when the output of the waveguide is perfectly matched:  $S_{11} = \frac{b_1}{a_1} \Big|_{a_2=0}$  and  $S_{21} = \frac{b_2}{a_1} \Big|_{a_2=0}$ . The transmission of the coplanar waveguide is  $-5.2 \pm 0.4$  dB within the range 1.5 – 2 GHz. This modest value of power transmission ( $\approx 30\%$ ) is attributed to losses in the in-vacuum leads, in the micrometric-sized gold wires that ensure connection to the chip's pads, and in the on-chip wires.

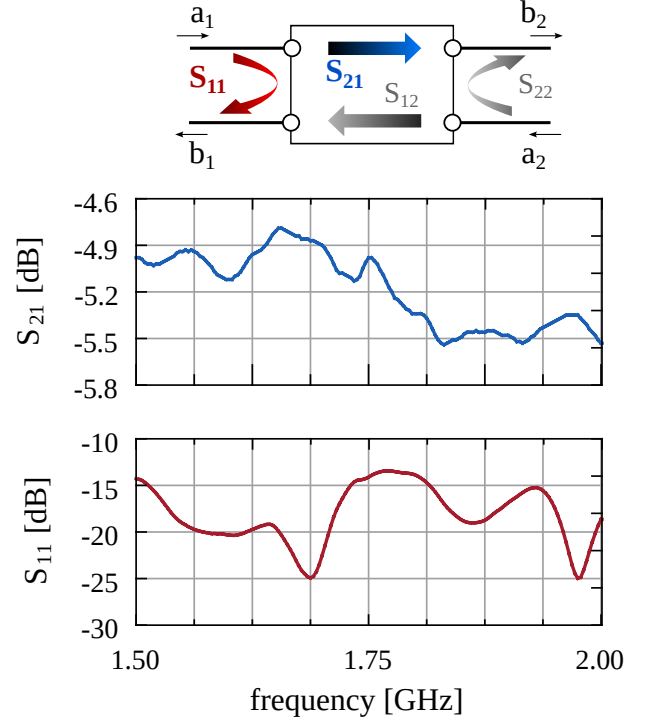


FIG. 12. Upper frame : scattering parameters of a 2-port device. Middle and lower frames : measured  $S_{21}$  and  $S_{11}$  parameters of the on-chip coplanar waveguide (CPW).

#### Appendix E: Microwave field coupling

The Hamiltonian describing the coupling of a sodium atom in its ground state with a microwave field in the presence of a static magnetic field can be split into two terms

$$\hat{H}(t) = \hat{H}_{\text{hfs}} + \hat{H}_{\text{B}}(t) \quad (\text{E1})$$

where

$$\hat{H}_{\text{hfs}} = \frac{\hbar\omega_{\text{hfs}}}{2} \frac{\hat{\mathbf{I}} \cdot \hat{\mathbf{J}}}{\hbar^2}, \quad (\text{E2})$$

$$\hat{H}_{\text{B}}(t) = \frac{\mu_{\text{B}}}{\hbar} \left( g_J \hat{\mathbf{J}} + g_I \hat{\mathbf{I}} \right) \cdot (\mathbf{B}_s + \mathbf{B}_{\text{mw}}(t)). \quad (\text{E3})$$

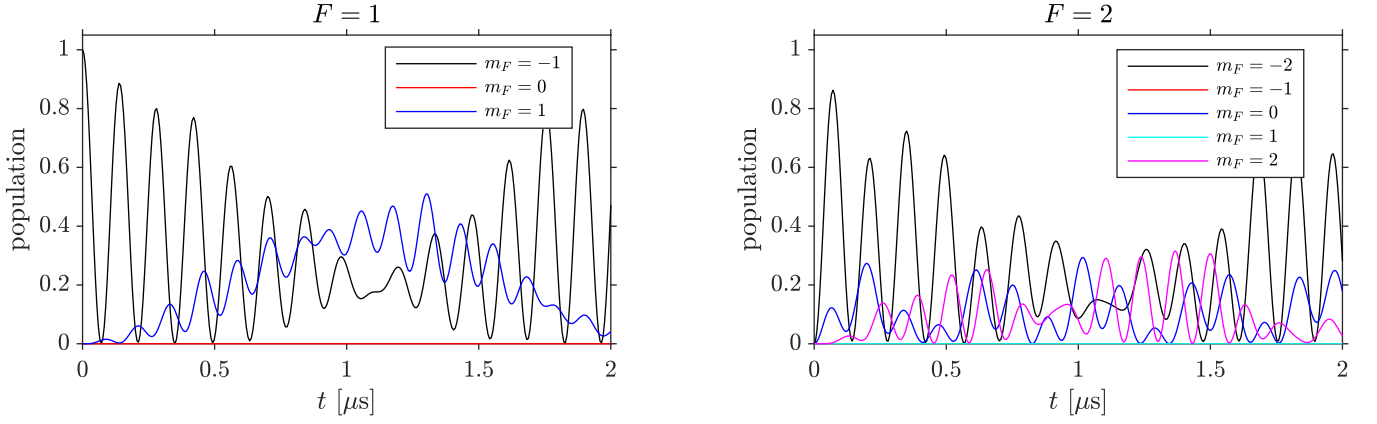


FIG. 13. **Left** - Coherent evolution of the population of the  $|F = 1, m_F\rangle$  states under the coupling with a microwave field taking into account the rotating wave approximation. We assume here that  $B_{\min} = 1$  G,  $B_X = 5.4$  G,  $B_Y = B_Z = 0$  G and  $\phi_X = \phi_Y = \phi_Z = 0$  which corresponds to a pure linear polarization. The microwave frequency  $\omega$  is chosen in order that the  $|F = 1, m_F = -1\rangle$  state is resonant with the  $|F = 2, m_F = -2\rangle$  state. All the atoms start in the  $|F = 1, m_F = -1\rangle$  state. **Right** - Same for the  $|F = 2, m_F\rangle$  states.

Here,  $\hat{\mathbf{I}}$  is the nuclear spin operator,  $\hat{\mathbf{J}}$  the total electronic spin operator,  $g_I$  the nuclear g-factor,  $g_J$  the Landé g-factor,  $\omega_{\text{hfs}} \simeq 2\pi \cdot 1771.6$  MHz the hyperfine splitting frequency,  $\mu_B$  the Bohr magneton,  $\mathbf{B}_s$  the external static field and  $\mathbf{B}_{\text{mw}}(t)$  the microwave field. Since the contribution from  $\hat{H}_B$  remains small compared to the hyperfine splitting energy in the situations we describe in this paper, we can write

$$\hat{H}_B(t) \simeq \frac{\mu_B}{\hbar} g_F \hat{\mathbf{F}} \cdot (\mathbf{B}_s + \mathbf{B}_{\text{mw}}(t)) \quad (\text{E4})$$

with  $\hat{\mathbf{F}} = \hat{\mathbf{I}} + \hat{\mathbf{J}}$  and  $|g_F| = 1/2$  the hyperfine Landé g-factor.

The most general expression for the microwave field

can be written as

$$\mathbf{B}_{\text{mw}}(t) = B_X \cos(\omega t + \phi_X) \mathbf{e}_X + B_Y \cos(\omega t + \phi_Y) \mathbf{e}_Y + B_Z \cos(\omega t + \phi_Z) \mathbf{e}_Z \quad (\text{E5})$$

where we have chosen the quantization axis  $\mathbf{e}_Z$  along the static field  $\mathbf{B}_s = B_{\min} \mathbf{e}_x$  such that  $\mathbf{e}_X \equiv \mathbf{e}_z$ ,  $\mathbf{e}_Y \equiv -\mathbf{e}_y$ ,  $\mathbf{e}_Z \equiv \mathbf{e}_x$ . We then introduce the unitary transform induced by the operator  $\hat{U}_{\text{hfs}}(t) = \exp(-i\omega t \hat{H}_{\text{hfs}}/\hbar\omega_{\text{hfs}})$ .

Applying  $\hat{U}_{\text{hfs}}$  to  $\hat{H}$  and neglecting all time-dependent terms according to the rotating wave approximation leads to

$$\hat{H}_{\text{eff}} = \hat{U}_{\text{hfs}}^\dagger \hat{H} \hat{U}_{\text{hfs}} - i\hbar \hat{U}_{\text{hfs}}^\dagger \frac{d\hat{U}_{\text{hfs}}}{dt} \simeq \frac{\hbar}{2} \begin{pmatrix} -5\delta + 2\delta_s & 0 & 0 & \sqrt{6}\Omega_-^* & \sqrt{3}\Omega_0^* & \Omega_+^* & 0 & 0 \\ 0 & -5\delta & 0 & 0 & \sqrt{3}\Omega_-^* & 2\Omega_0^* & \sqrt{3}\Omega_+^* & 0 \\ 0 & 0 & -5\delta - 2\delta_s & 0 & 0 & \Omega_-^* & \sqrt{3}\Omega_0^* & \sqrt{6}\Omega_+^* \\ \sqrt{6}\Omega_- & 0 & 0 & 3\delta - 4\delta_s & 0 & 0 & 0 & 0 \\ \sqrt{3}\Omega_0 & \sqrt{3}\Omega_- & 0 & 0 & 3\delta - 2\delta_s & 0 & 0 & 0 \\ \Omega_+ & 2\Omega_0 & \Omega_- & 0 & 0 & 3\delta & 0 & 0 \\ 0 & \sqrt{3}\Omega_+ & \sqrt{3}\Omega_0 & 0 & 0 & 0 & 3\delta + 2\delta_s & 0 \\ 0 & 0 & \sqrt{6}\Omega_+ & 0 & 0 & 0 & 0 & 3\delta + 4\delta_s \end{pmatrix}$$

where  $\delta = (\omega_{\text{hfs}} - \omega)/4$ ,  $\delta_s = |g_F| \mu_B B_{\min}/\hbar$  and  $\Omega_{0,+,-} = -|g_F| \mu_B B_{0,+,-}/\hbar$ . We have introduced  $B_+ = (-B_X e^{-i\phi_X} + iB_Y e^{-i\phi_Y})/\sqrt{2}$ ,  $B_- = (B_X e^{-i\phi_X} + iB_Y e^{-i\phi_Y})/\sqrt{2}$  and  $B_0 = B_Z e^{-i\phi_Z}$ , the  $\sigma_+$ ,  $\sigma_-$  and  $\pi$  components of the microwave field. The matrix is written in the basis  $\{|F = 1, m_F = -1\rangle, |F = 1, m_F = 0\rangle, |F = 1, m_F = 1\rangle, |F = 2, m_F = -2\rangle, \dots, |F = 2, m_F = 2\rangle\}$ . With these definitions, the microwave field can also be expressed as  $\mathbf{B}_{\text{mw}}(t) =$

$\frac{1}{2} [\mathcal{B} e^{-i\omega t} + c.c.]$  with  $\mathcal{B} = B_+ \mathbf{e}_+ + B_- \mathbf{e}_- + B_0 \mathbf{e}_Z$  and  $(\mathbf{e}_+, \mathbf{e}_-, \mathbf{e}_0)$  is the spherical basis :  $\mathbf{e}_+ = -(\mathbf{e}_X + i\mathbf{e}_Y)/\sqrt{2}$ ,  $\mathbf{e}_- = (\mathbf{e}_X - i\mathbf{e}_Y)/\sqrt{2}$ ,  $\mathbf{e}_0 = \mathbf{e}_Z$ .

In  $\hat{H}_{\text{eff}}$ , the off-diagonal coefficients directly correspond to the Rabi frequency of the population oscillations for a given transition between two hyperfine states [10]. The amplitude  $|\Omega_{0,+,-}|$  scales as  $2\pi \times 0.7 \text{ MHz} \cdot \text{G}^{-1}$  with the modulus of the corresponding component of the microwave field  $|B_{0,+,-}|$ .

It is now straightforward to compute numerically the evolution of the density matrix over time and a typical result is shown in Fig. 13, assuming a linear polarization of the microwave field,  $\phi_X = \phi_Y = \phi_Z = 0$ ,  $B_X = 5.4$  G and  $B_Y = B_Z = 0$  G. These parameters reproduces well the results observed in Fig. 9. The calculation clearly

shows that the decrease in the  $|F = 1, m_F = -1\rangle$  state at the maxima is due to an off-resonant coupling through the  $\sigma^+$  line to the  $|F = 2, m_F = 0\rangle$  state, which in turns populates the  $|F = 1, m_F = 1\rangle$  state through a  $\sigma^-$  line. The two-level approximation does not hold for this large field amplitude.

- 
- [1] J. Reichel, W. Hänsel, and T. W. Hänsch, Phys. Rev. Lett. **83**, 3398 (1999).
- [2] W. Hänsel, P. Hommelhoff, T. W. Hänsch, and J. Reichel, Nature **413**, 498 (2001).
- [3] J. Reichel, Appl. Phys. B **74**, 469 (2002).
- [4] R. Folman, P. Krüger, J. Schmiedmayer, J. Denschlag, and C. Henkel, Adv. At. Mol. Opt. Phys. **48**, 263 (2002).
- [5] J. Fortágh and C. Zimmermann, Rev. Mod. Phys. **79**, 235 (2007).
- [6] J. Reichel and V. Vuletić, eds., *Atom Chips* (Wiley, 2011).
- [7] M. Keil, O. Amit, S. Zhou, D. Groswasser, J. Yonathan, and R. Folman, Journal of Modern Optics **63**, 1840 (2016).
- [8] P. Treutlein, P. Hommelhoff, T. Steinmetz, T. W. Hänsch, and J. Reichel, Phys. Rev. Lett. **92**, 203005 (2004).
- [9] P. Böhi, M. F. Riedel, J. Hoffrogge, J. Reichel, T. W. Hänsch, and P. Treutlein, Nat. Phys. **5**, 592 (2009).
- [10] P. A. Böhi, *Coherent manipulation of ultracold atoms with microwave near-fields*, Ph.D. thesis, Ludwig-Maximilians-Universität München (2010).
- [11] C. Deutsch, F. Ramírez-Martínez, C. Lacroûte, F. Reinhard, T. Schneider, J. N. Fuchs, F. Piéchon, F. Laloë, J. Reichel, and P. Rosenbusch, Phys. Rev. Lett. **105**, 020401 (2010).
- [12] F. Ramírez-Martínez, C. Lacroûte, P. Rosenbusch, F. Reinhard, C. Deutsch, T. Schneider, and J. Reichel, Advances in Space Research **47**, 247 (2011), scientific applications of Galileo and other Global Navigation Satellite Systems - I.
- [13] L. Sárkány, P. Weiss, H. Hattermann, and J. Fortágh, Phys. Rev. A **90**, 053416 (2014).
- [14] R. Szmuk, V. Dugrain, W. Maineult, J. Reichel, and P. Rosenbusch, Phys. Rev. A **92**, 012106 (2015).
- [15] M. Ammar, M. Dupont-Nivet, L. Huet, J.-P. Pocholle, P. Rosenbusch, I. Bouchoule, C. I. Westbrook, J. Estève, J. Reichel, C. Guerlin, and S. Schwartz, Phys. Rev. A **91**, 053623 (2015).
- [16] M. Dupont-Nivet, M. Casiulis, T. Laudat, C. I. Westbrook, and S. Schwartz, Phys. Rev. A **91**, 053420 (2015).
- [17] B. Allard, M. Fadel, R. Schmied, and P. Treutlein, Phys. Rev. A **93**, 043624 (2016).
- [18] P. Colciaghi, Y. Li, P. Treutlein, and T. Zibold, Phys. Rev. X **13**, 021031 (2023).
- [19] D. J. Papoular, G. V. Shlyapnikov, and J. Dalibard, Phys. Rev. A **81**, 041603(R) (2010).
- [20] P. Cheiney, O. Carraz, D. Bartoszek-Bober, S. Faure, F. Vermersch, C. M. Fabre, G. L. Gattobigio, T. Lahaye, D. Guéry-Odelin, and R. Mathevet, Rev. Sci. Inst. **82**, 063115 (2011).
- [21] D. Ben Ali, T. Badr, T. Brézillon, R. Dubessy, H. Perrin, and A. Perrin, J. Phys. B **50**, 055008 (2017).
- [22] M. Greiner, I. Bloch, T. W. Hänsch, and T. Esslinger, Phys. Rev. A **63**, 031401(R) (2001).
- [23] T. Badr, D. Ben Ali, J. Seaward, Y. Guo, F. Wiotte, R. Dubessy, H. Perrin, and A. Perrin, Appl. Phys. B **125**, 102 (2019).
- [24] S. Dettmer, D. Hellweg, P. Ryytty, J.J. Arlt, W. Ertmer, K. Sengstock, D. S. Petrov, G. V. Shlyapnikov, H. Kreutzmann, L. Santos, and M. Lewenstein, Phys. Rev. Lett. **87**, 160406 (2001).
- [25] A. Imambekov, I. E. Mazets, D. S. Petrov, V. Gritsev, S. Manz, S. Hofferberth, T. Schumm, E. Demler, and J. Schmiedmayer, Phys. Rev. A **80**, 033604 (2009).
- [26] M. Schemmer, A. Johnson, and I. Bouchoule, Phys. Rev. A **98**, 043604 (2018).
- [27] F. Dalfovo, S. Giorgini, L. P. Pitaevskii, and S. Stringari, Rev. Mod. Phys. **71**, 463 (1999).
- [28] F. Gerbier, Europhys. Lett. **66**, 771 (2004).
- [29] B. M. Garraway and H. Perrin, J. Phys. B **49**, 172001 (2016).
- [30] S. Hofferberth, B. Fischer, T. Schumm, J. Schmiedmayer, and I. Lesanovsky, Phys. Rev. A **76**, 013401 (2007).
- [31] C. Maury, B. Bakkali-Hassani, G. Chauveau, F. Rabec, S. Nascimbene, J. Dalibard, and J. Beugnon, Phys. Rev. Research **5**, L012020 (2023).
- [32] W. Ketterle, D. S. Durfee, and D. M. Stamper-Kurn, in *Proceedings of the International School of Physics "Enrico Fermi" Volume 140: Bose-Einstein Condensation in Atomic Gases* (1999) pp. 67–176.
- [33] D. A. Steck, Sodium D Line Data, available online at <http://steck.us/alkalidata> (revision 2.3.2, 10 September 2023).
- [34] Y. Castin and R. Dum, Phys. Rev. Lett. **77**, 5315 (1996).